TU Delft

Delft University of Technology

Document Version
Final published version

Licence
CC BY

Citation (APA)
Fricke, L. V., Wansink, N., Rosso, M., van Ewijk, G., Smak, M. P., Belardinelli, P., Staufer, U., & Alijani, F. (2026). Nanomechanical degradation of a waterborne acrylate coating due to accelerated weathering revealed by atomic force microscopy. *Polymer Degradation and Stability*, *254*, Article 112475. https://doi.org/10.1016/j.polymdegradstab.2026.112475

Important note
To cite this publication, please use the final published version (if applicable).
Please check the document version above.

Copyright
In case the licence states “Dutch Copyright Act (Article 25fa)”, this publication was made available Green Open Access via the TU Delft Institutional Repository pursuant to Dutch Copyright Act (Article 25fa, the Taverne amendment). This provision does not affect copyright ownership.
Unless copyright is transferred by contract or statute, it remains with the copyright holder.

Sharing and reuse
Other than for strictly personal use, it is not permitted to download, forward or distribute the text or part of it, without the consent of the author(s) and/or copyright holder(s), unless the work is under an open content license such as Creative Commons.

Takedown policy
Please contact us and provide details if you believe this document breaches copyrights.
We will remove access to the work immediately and investigate your claim.

This work is downloaded from Delft University of Technology.

Polymer Degradation and Stability 254 (2026) 112475

Contents lists available at ScienceDirect

Polymer Degradation and Stability

journal homepage: www.journals.elsevier.com/polymer-degradation-and-stability

Nanomechanical degradation of a waterborne acrylate coating due to accelerated weathering revealed by atomic force microscopy

L.V. Fricke [a,*], N. Wansink [a], M. Rosso [b], G. van Ewijk [b], M.P. Smak [a], P. Belardinelli [c], U. Staufer [a], F. Alijani [a,*]

[a] Department of Precision and Microsystem Engineering, Delft University of Technology, 2628CD Delft, The Netherlands
[b] AkzoNobel, 2171AJ Sassenheim, The Netherlands
[c] Department of Construction, Civil Engineering and Architecture, Polytechnic University of Marche, 60131 Ancona, Italy

ARTICLE INFO

Keywords:
Waterborne coating
Accelerated weathering
Nanoscopic analysis
Degradation mechanism
Atomic force microscopy

ABSTRACT

Waterborne polymer coatings are increasingly used as sustainable alternatives to solvent-borne systems, but their long-term durability remains a challenge. Elucidating their degradation mechanism at the nanoscale, where damage first emerges, is essential for delivering more durable waterborne coatings. Here, we use intermodulation atomic force microscopy (ImAFM) to investigate the nanoscale origins of degradation in an accelerated weathered waterborne acrylate coating. Our measurements reveal a progressive, three-stage degradation pathway induced by accelerated weathering. In the first stage, the coating stiffens as a result of physical aging and (photo-)chemically induced degradation. Subsequently, former acrylate particles re-emerge and become surrounded by regions of increased damping and reduced stiffness. Continued weathering eventually gives rise to pronounced viscoelastic heterogeneity. To support these observations, we performed both bulk and nanoscale dynamic mechanical analysis measurements on accelerated weathered samples. These measurements reveal increased storage modulus and damping, consistent with the nanoscale evolution observed by ImAFM. Together, these results identify the mechanical changes that precede macroscopic embrittlement and demonstrate that durability limitations in waterborne acrylate coatings are strongly linked to the development of localized viscoelastic heterogeneity at the nanoscale.

1. Introduction

Modern polymeric coatings are shifting towards waterborne systems to minimize harmful environmental emissions. As a result, they gain substantial commercial uptake in large sectors such as architectural and automotive industry. Nevertheless, their performance still lags behind conventional solvent-borne systems [1]. Exposure to UV radiation, temperature changes, moisture, and oxygen, induces chemical and physical transformations in coatings, including chain scission, (photo-)oxidation, radical formation, and network restructuring. Such molecular-scale processes lead to degradation and manifest macroscopically as gloss and color loss, cracking, chalking, and blistering [2–6].

Coatings degradation typically begins at the surface on the nanoscale and progressively propagates through the bulk [5,7]. Although surface degradation may be tolerated in certain protective applications, it can signal an underlying damage process. This effect can be amplified by formulation heterogeneity, where non-uniformly distributed components create localized mechanical contrasts and weak interfaces that promote crack initiation and subsequent propagation. Ultimately, this can lead to a progressive loss of the protective and aesthetic functions of coatings [8]. These considerations are especially relevant to waterborne coatings, which are intrinsically heterogeneous by design [9,10]. Unlike solvent-based coatings, where polymeric components are molecularly dissolved and form a molecular homogeneous film, waterborne coatings consist of discrete polymer particles dispersed within a continuous aqueous phase, resulting in a compartmentalized microstructure. These waterborne coatings can show a morphological homogeneity but on the molecular level there are still signs of the former particles due to different connections between the particles and molecular bindings and entanglements inside the particles [11,12]. Consequently, understanding the onset and progression of degradation in waterborne coatings requires characterization techniques capable of resolving nanoscale heterogeneity and its evolution during environmental exposure. Despite their widespread use, conventional bulk characterization techniques such as dynamic mechanical analysis (DMA) [13], only yield spatially averaged viscoelastic

* Corresponding authors.
E-mail addresses: l.v.fricke@tudelft.nl (L.V. Fricke), f.alijani@tudelft.nl (F. Alijani).

https://doi.org/10.1016/j.polymdegradstab.2026.112475
Received 30 June 2026; Received in revised form 10 September 2026; Accepted 19 September 2026
Available online 26 September 2026
0141-3910/© 2026 The Authors. Published by Elsevier Ltd. This is an open access article under the CC BY license (http://creativecommons.org/licenses/by/4.0/).

responses and therefore lack sensitivity to early-stage, nanoscale degradation which can be caused by heterogeneous microstructure. For instance, coatings with distinct UV exposure histories may exhibit comparable loss modulus behavior, masking differences in degradation state and mechanism, as reported in [7]. Environmental exposure often activates multiple degradation pathways that may occur simultaneously or sequentially, with their individual effects masked in bulk measurements. In addition, nanoscale structural changes can act as initiation sites for macroscopic degradation, highlighting the need for characterization methods capable of capturing nanomechanical processes during material evolution [14].

In this work, we investigated the degradation of an acrylate waterborne coating, undergone accelerated weathering, at the nanoscale to resolve its early-stage nanomechanical changes. Previous atomic force microscopy (AFM) studies have already shown that UV exposure induces pits and inhomogeneous nano- to micro-scale domains [5]. However, while the most commonly used dynamic AFM methods can access local properties, quantitative mechanical information is out of reach [15,16]. Hence, the nanomechanical consequences of these structural changes and their role in coating degradation remain poorly understood. Intermodulation AFM (ImAFM) overcomes these limitations by enabling high-sensitivity mapping of surface morphology while simultaneously providing quantitative nanoscale mechanical characterization [15,16]. To determine the nanomechanical properties, in this study we combined ImAFM with low-frequency nanoscale viscoelastic measurements that probe the local response in a manner analogous to DMA. This approach enables direct monitoring of the evolution of structural and nanomechanical heterogeneity during weathering. We show that degradation is initiated by the re-emergence of former acrylate particles surrounded by regions with enhanced loss tangent. With continued accelerated weathering, we show that these localized changes develop into pronounced viscoelastic heterogeneity characterized by mechanically weak domains. Together, these observations reveal how the intrinsic heterogeneity of waterborne coatings governs the onset of localized embrittlement and ultimately limits coating durability.

2. Materials & methods

2.1. Coating production

The waterborne coating was prepared by mixing 60 wt% of a commercial acrylate binder (Primal AC337DS, Dow Chemicals) with water (16 wt%) and several additives (24 wt%) consisting of rheology modifier, co-solvents, surfactants and anti-microbial preservatives. The acrylate binder included 45 wt% solids of an acrylate polymer dispersed in water, with a minimal film formation temperature (MFFT) of about 14 °C, based on the technical sheet information. When excluding water and organic co-solvents from the recipe, the calculated residual solid content of the formulation was about 33% w/w, of which 29% was the binder. All ingredients were incorporated one by one under mechanical stirring with a table mixer (2500 rpm), starting with water and the acrylate binder. After at least 24 h of storage, the liquid formulation was applied on primed aluminum and on bare polypropylene panels with a wired bar (k-bar 7) on an automatic applicator to reach a dry coating film thickness of 32 ± 1 μm.

In Fig. 1 the curing process is summarized. The latex film formation is also described in more detail in [9]. For most water-based acrylate emulsion binders, emulsion polymerization is used, where acrylate monomers are first emulsified before starting the polymerization. Due to the hydrophobic properties of the monomers, a monomer droplet surrounded by surfactant molecules is created inside an aqueous environment (step 1). The polymerization of the monomer then results in particles with a typical size of 50 to 200 nm (step 2). Subsequently, the waterborne binder is formulated and applied to a surface; the wet film dries (step 3) and the particles arrange in a close particle packing (step 4), with a particle size of less than 100 nm in our case. An AFM topography and phase image of the unformulated binder is presented in Fig. 1, revealing the presence of separated acrylate particles. A similar morphology in early-stage polymer films has been reported in [12], where AFM height images of a freshly applied polymer film resemble the phase image observed here for the unformulated binder. Lastly, a particle deformation process due to surface minimization effects takes place (step 5). The liquid films were left to dry in ambient conditions for 24 h, and later for at least two days at 50 °C, which is above the stated Minimum Film Forming Temperature (MFFT) of this formulation as well as the coatings' glass transition temperature T_g, that has been estimated to be 40 °C via DMA (cf. SI [17], reference state) according to the tan δ method. Here, the particle coalesce and an optical homogeneous film is formed (step 6). The coalescence of particles is only observed visibly (transparent films), when the drying temperature is above the MFFT of the binder. Performing a forced drying above T_g, ensures that particle coalescence is achieved to an even higher extent. Then, an interpenetration of chains may happen so that a continuous film is formed [10].

2.2. Accelerated weathering

To assess coating degradation, accelerated weathering protocols are commonly used that expose coatings to a combination of environmental stressors, including temperature cycling, UV radiation, oxygen exposure, and humidity. The extent of degradation is strongly environment-dependent, with UV exposure producing more severe chemical and mechanical changes than thermal aging alone [18]. The durability of the coatings analyzed in this study was evaluated using accelerated weathering in a xenon arc Weather-O-Meter (WOM). The exposure cycle followed ISO 16474-2 (Method A, Cycle 1) [19], ISO 4892-2 (Method A, Cycle 1) [20], and Volkswagen PV 3930 [21]. Samples were applied on aluminum sheets (these samples were used for AFM testing) and polypropylene sheets, where it was possible to peel-off the coatings for DMA measurements. The specimens were subjected to alternating dry and wet periods under simulated sunlight, controlled temperature, water spray, and relative humidity. During the dry period, specimens were exposed for 102 min at a black standard temperature of 65 ± 2 °C, chamber temperature of 38 ± 3 °C, relative humidity of 55 ± 5%, and an irradiance of 0.51 ± 0.01 W m^{-2} nm^{-1} at 340 nm. The wet period consisted of an 18 min front spray at a black standard temperature of 38 ± 3 °C and relative humidity of 95 ± 5%, while maintaining constant irradiance. Exposure was performed using a 6.5 kW or 12 kW xenon lamp equipped with borosilicate (inner/outer) filters, within the specified tolerances of the referenced standards.

2.3. AFM

All AFM experiments were conducted in an environmental chamber, and nanomechanical characterization experiments were performed at a constant humidity of approximately 10%, regulated by flushing the chamber with dried air. This reduces the effects of adhesive and capillary forces due to adsorption of water on the polymeric surface [22,23]. The temperature for all AFM measurements was set at 20 °C using a Peltier element-based controller (Meerstetter Engineering GmbH) since the properties of the viscoelastic material are strongly temperature dependent.

The topography images were acquired using a commercial AFM (Nanosurf GmbH, DriveAFM), operating in a standard dynamic mode, where the cantilever was vibrating close to its resonance and the modulation of its amplitude was used to control the tip sample interaction. All measurements were conducted using rectangular silicon cantilevers by NanoAndMore, the Tap190Al-G. The cantilever properties were determined before each measurement by using the thermal calibration based on the Sader's method [24,25]. The properties were in the range of k = 14.5–27 N/m, f_0 = 162–168.6 kHz, and Q = 308–549. The tip radius was 10 nm (according to the manufacturer). A line-scan rate of

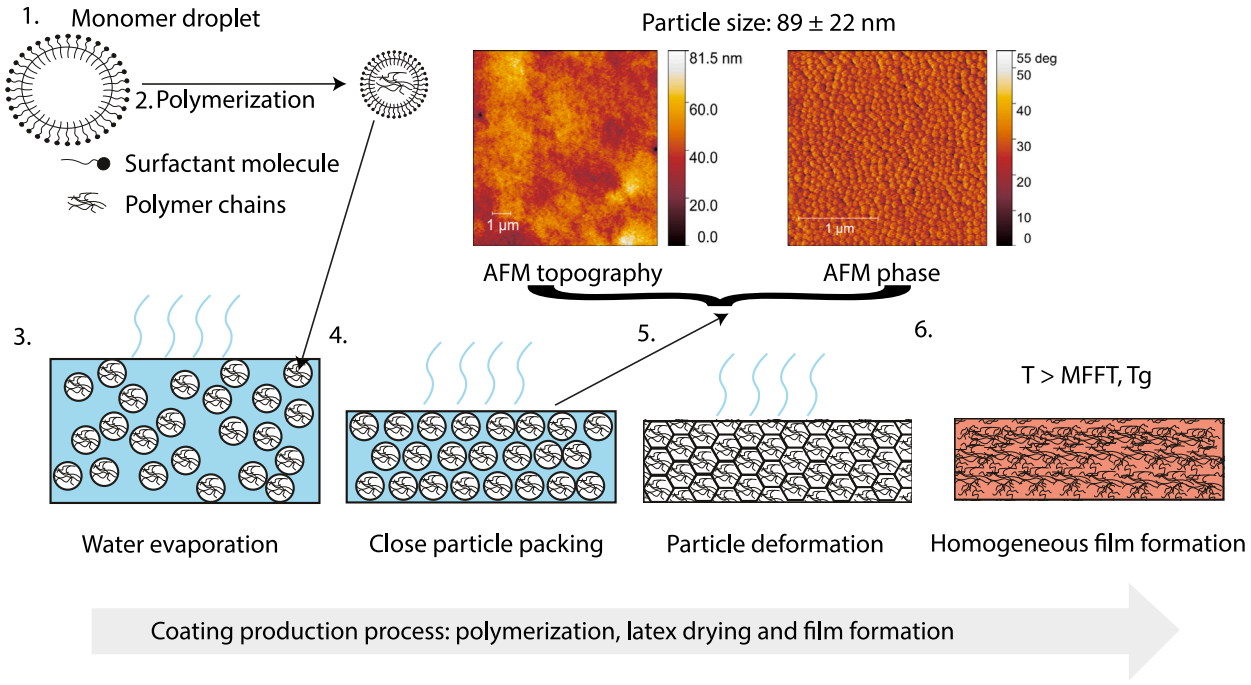


Fig. 1. Waterborne acrylate latex coating curing process. First monomer droplets are dispersed into water using a surfactant. Inside the droplets, which have a size of approximately 100–200 nm, the polymerization (step 2) takes place. Step 3–6 show the film formation process. By heating the film over T_g, polymer chain connection between the former particles are created. The AFM pictures show the topography and AFM cantilever phase of the binder before step 5 and 6.

1 Hz was set, and AFM images were obtained at different dimensions with a resolution of 500 × 500 pixels. The surface roughness was determined by using Gwyddion (Opensource). The displayed values are the average values of five lines across the whole image width of three images.

The ImAFM experiments were performed using the same AFM instrument as for imaging, however in this case combined with a multi lock-in amplifier (MLA) (Intermodulation Products AB). The MLA was used to measure, control and analyze the frequency components resulting from the tip-sample interaction. In ImAFM measurements, the cantilever was excited by two tones (f_1 and f_2) equidistant from its fundamental resonance frequency (f_0). The interaction of the cantilever with the sample generates intermodulation products (IMP), i.e., equally spaced tones or frequency peaks with a distance equal to the mechanical bandwidth $\delta f = f_0/Q$. A detailed explanation of ImAFM as a technique is provided in [26–29]. The occurrence of such IMPs is dependent on the material properties. In the SI [17], for example Figure S5 shows the influence of the accelerated weathering time on the IMPs.

To extract the viscoelastic properties, the tip-sample force was analyzed based on its in-phase and out-of-phase components, knowing the amplitude and phase of intermodulation products and following the procedure detailed out in our earlier work [30]. These components of the tip-sample force are only affected by the respective conservative and dissipative parts of the interaction [28]. More information about the viscoelastic material property retrieval procedure based on the measured in-phase and out-of-phase components and simulated ones can be found in the SI [17] in chapter S3.

To probe the viscoelastic properties of coatings using ImAFM, we model the sample as a Kelvin–Voigt solid [15,31] and use long-range nonlinear van der Waals (non-contact) and Derjaguin–Muller–Toporov (contact) forces to account for tip-sample interactions [32]. This leads to the following expression for the force between the cantilever tip and the sample F_{ts}

$$F_{ts}(z) = \begin{cases} -\dfrac{HR}{6z^2}, & \text{for } z > a_0, \\ -\dfrac{HR}{6a_0^2} + \dfrac{4}{3}E^{\dagger}\sqrt{R}\,\upsilon^{3/2} + \psi\sqrt{R}\sqrt{\upsilon}\,\dot{\upsilon}, & \text{for } z \le a_0. \end{cases} \tag{1}$$

in which $z(t)$ is the instantaneous tip-sample separation, measured from the sample, a_0 the intermolecular distance, and $\upsilon = a_0 - z$ is the sample indentation. Eq. (1) indicates a purely attractive regime (F_{nc}) for the cantilever ($z > a_0$), where the interaction is influenced by the Hamaker constant H and the tip radius R. When $z \le a_0$, the regime of contact is entered (F_c). Here, in addition to the adhesion $F_{nc}|_{z=a_0}$, a repulsive force proportional to the effective Young's modulus $E^{\dagger}$, and the square root of the tip radius is present. The effective Young's modulus is commonly known as the contact elasticity, which is composed of the elasticity of the sample and the tip [33]. Since, in our case the deformation of the tip is negligible compared to the one of the sample, $E^{\dagger} = \dfrac{E_s}{1-\nu_s^2}$ where E_s and ν_s are the Young's modulus and the Poisson's ratio of the sample, respectively.

For most elastic materials, contact elasticity describes the amount of energy stored within the material. This can be compared to the elastic component of viscoelastic materials, known as the storage modulus E' [34]. The purely elastic behavior exhibits no frequency dependence, and in our model is related to the component $\frac{4}{3}E^{\dagger}\sqrt{R}$. However, in contrast to purely elastic materials [35], viscoelastic materials require a model that accounts for a velocity-dependent viscous component. This component is proportional to the viscosity parameter ψ, capturing the dissipative nature of the material [31]. The loss component for viscoelastic materials (loss modulus E'') stems from the friction force in Eq. (1) that is $\psi\sqrt{R}\sqrt{\upsilon}\dot{\upsilon}$. The ratio of energy loss to energy storage defines the loss tangent, expressed as $\tan\delta = \frac{E''}{E'}$ in terms of the mechanical properties of the material, and is calculated via:

$$\tan\delta = \frac{\langle F_{ts}\cdot\dot{z}\rangle}{\omega\langle F_{ts}\cdot z\rangle}, \tag{2}$$

where the $\langle\rangle$ represent a time average [36].

The relation of the loss tangent with the material parameters is:

$$\tan\delta = \frac{\omega}{2}\frac{\psi}{E^{\dagger}}. \tag{3}$$

More information about the retrieval of Eq. (3) can be found in [37].

The cantilever was opto-thermally driven using an intensity modulated laser diode with a power of 8 mW. ImAFM images were obtained at different sizes with a resolution of 256 × 256 pixels.

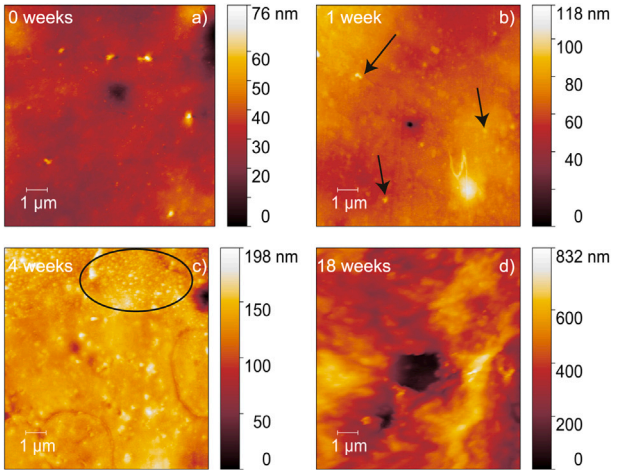


Fig. 2. Topography images, captured using dynamic AFM. The evolution of the surface topography over accelerated weathering time is depicted. (a) Initial state, (b) 1 week accelerated weathering, (c) 4 weeks accelerated weathering, (d) 18 weeks accelerate weathering. Note that the scale is adjusted to every picture so that as many details as possible can be observed. An increase in topological features like round spots (see arrows and marked region) with increasing accelerated weathering time is visible.

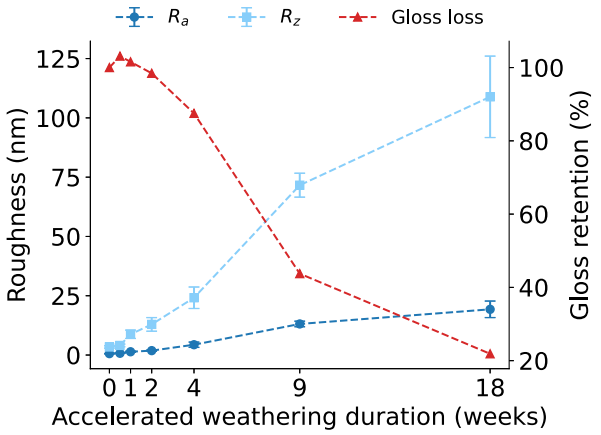


Fig. 3. Roughness values R_a and R_z and gloss loss (initial value amounts to 64 GU) over accelerated weathering duration (estimated via AFM — see Section 2.3 and quantified using a specular glossmeter — see Section 2.5). With increasing weathering duration the surface roughness increases and the gloss decreases.

To complement the ImAFM measurements, we performed nanoscale dynamic mechanical analysis using the VEA module of DriveAFM from Nanosurf. This technique probes the local viscoelastic response through low-frequency oscillatory excitation, analogous to nano-DMA [38,39]. In this mode, the cantilever tip is brought into contact with the material, and after a relaxation period, it is driven at different frequencies. The force needed is recorded and the phase difference between the actuation and the measured response gives information about the viscoelastic material properties. The evaluation model to translate deflection information into mechanical properties is based on a spherical Hertz model. At each measurement position, ten VEA measurements were performed. Afterwards the tip deflection $y(\omega)$ and indentation $\delta(\omega)$ was gained from frequency fits. More detailed information can be found in the SI [17] in Figure S7. The equation used to convert the raw data into nanomechanical properties was based on the method described by Rebêlo et al. [40], as follows:

$$E^*(\omega) = \frac{(1-\nu)k_c}{2\sqrt{R\cdot\delta_0}} \cdot \frac{y(\omega)}{\delta(\omega)} \tag{4}$$

where ν is the Poisson's ratio (set to 0.4), k_c is the cantilever stiffness, R is the tip radius, and δ_0 is the equilibrium indentation depth. Thereby, the storage modulus E' is the real part of the complex modulus E^* and the loss modulus E'' the imaginary part. The cantilever for these measurements was actuated by a z-piezo. Since the force evaluation of VEA is strongly dependent on the deflection sensitivity determined in the calibration process, an additional calibration was conducted before VEA measurements. The deflection sensitivity was calibrated on a hard silicon sample were a force distance grid of 10 × 10 µm was measured. The lowest slope of the retracted curve was taken as deflection sensitivity.

2.4. DMA

The bulk viscoelastic behavior of the coatings was assessed on a Q800 (TA instruments) in tensile mode. To ensure the samples are deformed in the linear viscoelastic region (LVR), where the characterized viscoelastic parameters of the materials are independent of the applied strain, a strain sweep was first performed to determine the linear strain range. The strain sweep was conducted at 30 °C at 10 Hz. A strain amplitude of 0.02% was selected from the strain sweep for the following temperature sweep which is a type of oscillatory testing in DMA, that deforms the rectangle-shaped coating samples sinusoidally as a function of temperature. The gauge length of the specimen used in the measurement was between 4–5 mm. Each measurement was performed on a fresh specimen, and the specimen was constantly tensioned to prevent buckling by applying an axial force of 0.2 N. The temperature sweep increased the temperature by 5 °C per step, and multi-frequencies from 10 Hz to 150 Hz were applied at each temperature step. The temperature range was between −20 °C to 80 °C. The upper boundary of 80 °C in the latter range was as close to the glass transition temperature T_g as the force resolution limit of the machine would allow. Results of these measurements are also presented in [17] Figure S3. The thickness of the samples was measured using a commercially available optical profilor (Bruker Contour GT-K).

2.5. Gloss loss measurements

Surface gloss was quantified using a specular glossmeter (BYK Instruments) at three geometries (20°, 60°, and 85°) in accordance with internationally standards ISO 2813 [41] and ASTM D523 [42]. Gloss is defined as the ratio of specularly reflected light from a test surface to that from a reference standard with a refractive index of 1.567 at a wavelength of 589 nm, with results reported in gloss units (GU) with an uncertainty of ±1 GU.

2.6. Photo-oxidation product analysis by FTIR-ATR

Chemical degradation of coatings during weathering was evaluated by monitoring the formation of photo-oxidation products (POP) using Fourier Transform Infrared spectroscopy in attenuated total reflectance (FTIR-ATR) mode. Photo-oxidative degradation was assessed by following the buildup of hydroxy (–OH) and acid (–COOH) functional groups relative to the remaining organic binder. Infrared spectra were collected directly from coated surfaces, and POP values were calculated by integrating the combined –OH/–NH stretching region (3500–2500 cm^{-1}) and normalizing it to the C–H stretching region (3120–2760 cm^{-1}), which serves as an internal reference for film thickness and residual organic content. The POP signal was defined as the increase in the normalized –OH/–NH contribution relative to the initial (unexposed) state. The evolution of POP as a function of exposure time was used as a qualitative indicator of the photo-oxidation rate, enabling early assessment of coating durability prior to the appearance of macroscopic damage such as gloss loss, cracking, or discoloration.

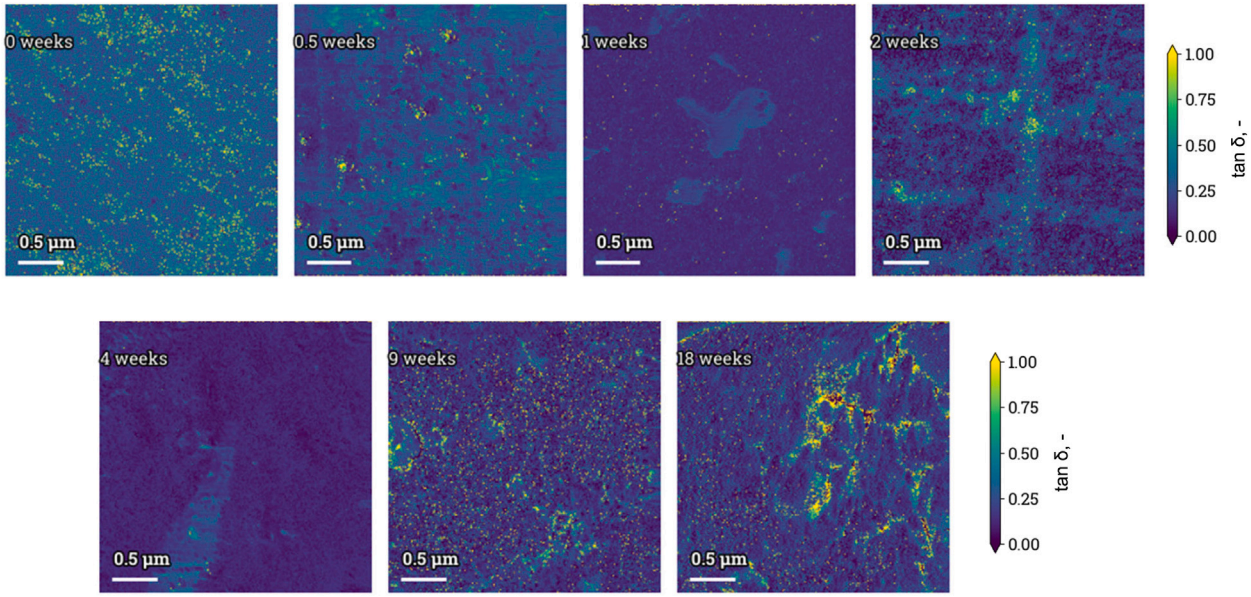


Fig. 4. Spatial distribution of the loss tangent tan δ evolution over accelerated weathering duration. With increasing weathering time areas with high damping properties (high loss tangent values, yellow) appear.

3. Results and discussion

3.1. Evolution of coating topology

The investigated waterborne acrylate coatings visibly exhibits a homogeneous film formation (clear transparent films), and no residual acrylate particles were detectable with the AFM after curing, see Fig. 2(a). We monitored the evolution of R_a (average roughness) and R_z (mean roughness depth) and observed that they increase over the weathering duration (see Fig. 3).

The roughness increase is approximately linear and is attributed to the apparition of particles along with other emerging topological features, which start to appear as isolated hillocks of few tens of nanometer in height after one week of accelerated weathering time (Fig. 2(b)) and are more pronounced after four weeks of accelerated weathering time, see Fig. 2(c). More AFM topography and phase images of all accelerated weathering steps analyzed in this study can be found in the supporting information [17] in Figure S1 and S2.

Alongside the increase in roughness, the sample experiences a macroscopic loss of gloss (triangle markers in Fig. 3). This effect is a byproduct of the roughness increase, as already reported in literature (see e.g. [43]). A slight increase in gloss at 0.5 weeks might be related to some loss of surfactant, as previously reported in other studies on gloss-loss such as in [44]; however, no clear explanation for this increase has been proposed. For unpigmented waterborne coatings, Vink et al. observed a significant gloss loss after approximately three weeks [45], which is comparable to our findings.

Next to the already mentioned increase in roughness, AFM measurements also revealed the appearance of round features (see 2(b)). Similar protuberances have been observed during the early degradation stages of epoxy coatings investigated by AFM [46]. This early topographical evolution precedes significant macroscopic gloss loss, which becomes pronounced after approximately four weeks of exposure. After this period, many accumulations of these round features were found, as it can also be seen in Fig. 2(c). Similar early-stage roughening has been associated with the onset of selective degradation and evolving microstructural heterogeneity in waterborne coatings [47]. Furthermore, exposure to UV radiation and high relative humidity has previously been shown to induce surface roughening and pit formation in polymeric coatings [48], supporting the interpretation that the observed topographical changes represent early stages of weathering-induced surface degradation.

The consistent gloss reduction at four weeks of accelerated weathering time, reflects the cumulative effect of nanoscale roughening evolving into microscale roughness changes, which is sufficient to enhance diffuse light scattering. This progression from nanoscopic changes to macroscopic degradation has also been reported for different coating systems including solvent borne polyurethane under accelerated weathering [2].

3.2. Emergence of highly damped nanoscale areas

To further analyze the local nanomechanical changes caused by the degradation process, ImAFM images of each accelerated weathering stage with a size of 2.5 µm × 2.5 µm were taken. In Fig. 4, the measured loss tangent tan δ is presented as function of location using a color code. It can be seen that after nine weeks of accelerated weathering, and particularly after 18 weeks, nanoscale regions with locally increased loss tangent values were detected: a higher proportion of the energy is dissipated rather than stored. In the SI [17] Figure S6 the according effective Young's modulus maps can be found. Since we did not monitor the tip degradation, we used the nominal tip radius provided by the manufacturer. Based on earlier studies (see [37,49]) for the material model used here, we assume an uncertainty of roughly 5% due to a possible change in tip radius.

Close-up images with a size of 1 µm × 1 µm show the appearance of highly damped areas in more detail in Fig. 5. The distribution of mechanical data derived from these measurements as well as another area on the same samples are shown in Figure S10 in the SI. These dissipative regions coincided with lower stiffness areas compared to the surrounding matrix, as marked with red arrows. This observation suggests localized structural breakdown. Especially noticeable in the loss tangent distribution after nine weeks of accelerated weathering, low-damping areas become observable, which resemble particles embedded in areas of higher damping. This is particularly visible in the left upper corner of Fig. 5(a). By taking the average of 15 measurements, an average particle size of 95 ± 88 nm was determined. The unformulated binder shows a particle size of 89 ± 22 nm, which is also stated in Fig. 1. The highly damped regions are, on average, slightly larger than the original particle size. A plausible mechanism of the creation of

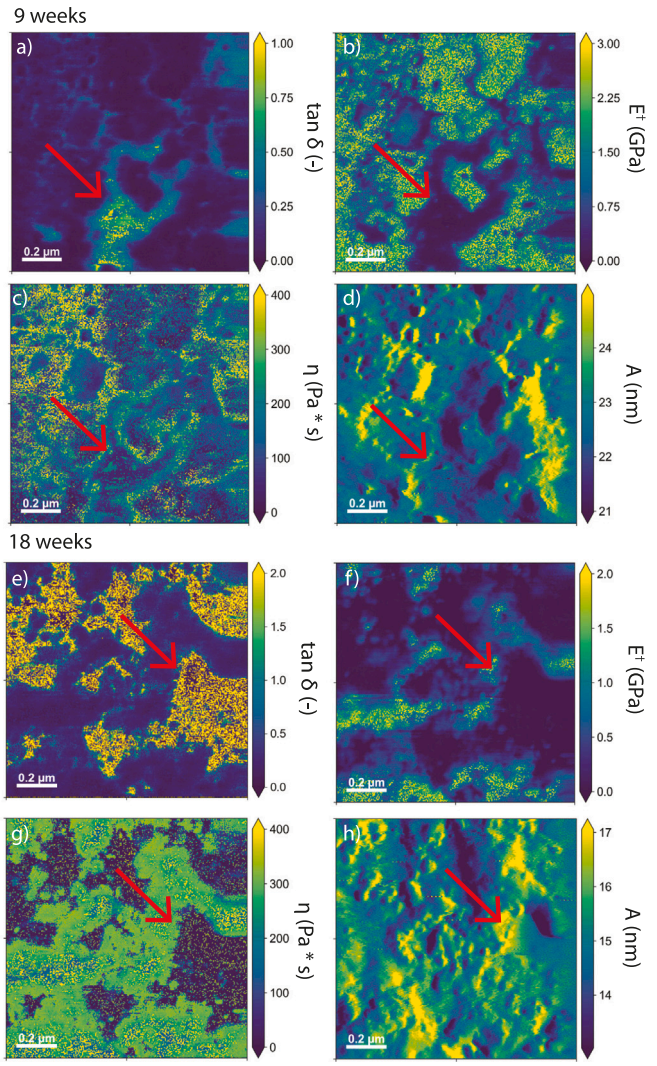


Fig. 5. 1 µm × 1 µm images of highly damped areas which were first detected after 9 weeks (a–d) and are more pronounced after 18 weeks (e–h) of accelerated weathering. The arrow marks the same areas in the loss tangent tan δ (a+e), E-modulus (b+f), viscosity (c+g) and cantilever amplitude (d+h) of the first drive tone of ImAFM measurement for 9 and 18 weeks weathering duration.

these highly damped pathways is the cleavage of interparticle polymer bridges formed during film formation above MFFT. Although particle–particle interfaces seem initially eliminated via chain inter-diffusion and entanglement, the interface can be inherently heterogeneous due to a lower chain entanglement between former acrylate particles than inside the particles themselves. Weakly entangled domains, characterized by higher mobility and water uptake, are particularly susceptible and act as preferential degradation sites. This supports the hypothesis that regions between former acrylate particles serve as initiation points for degradation. Under UV exposure, degradation starts preferably locally at weak nanoscale sites [5]. Accelerated weathering studies on waterborne acrylate nanocomposites show selective interfacial degradation and nanoscale phase separation [47], while oxidative degradation in polyurethane coatings leads to micro-crack initiation in mechanically weakened zones [2]. Consistently, earlier AFM studies already reveal that UV degradation proceeds in a localized manner, forming nanoscale pits that grow in size and depth over time [5]. Morsch et al. observed a heterogeneous degradation due to the distribution of cross-linking density in epoxy resins which leads to locally enhanced water uptake in regions of lower cross-linking density [50]. With increasing weathering time, the area fraction of highly damped areas increases significantly from below 1% to over 6%. This can also be seen in Figure S10 in the SI.

We therefore propose that former particle boundaries act as latent weak points enriched in high-cross-linked domains. These compliant nanoscale regions act as stress concentrators within a stiff oxidized matrix, promoting strain localization and brittle failure. Failure propagation may thus follow these predefined high damped interfacial pathways, consistent with the localized pit growth observed during degradation by Nguyen et al. [5]. Chain scission hence, may reduce entanglement density across these regions, which may enable the re-emergence of particle-like domains with elevated viscoelastic property. Of course, as it can be seen in the bigger area size of re-emerging particles compared to the original particle size in Fig. 1, not every connection between former particles was degraded. Further, we cannot completely exclude that the observed round features and high-damping regions could also arise from other degradation mechanisms such as surfactant loss or heterogeneous oxidation.

3.3. Evolution of (nano)mechanical properties

ImAFM further revealed a systematic increase in effective Young's modulus at the microscale with increasing weathering duration (compare Fig. 6(a)). Concurrently, the histogram, which represent the normalized amount of counts (pixels) of the effective Young's modulus values, broadens and shifts toward higher stiffness. The shift to higher values is consistent with surface oxidation and hence, the creation of more polar regions, which restrict segmental mobility and increase local stiffness [47]. However, the broadening of the effective Young's modulus distribution indicates growing mechanical heterogeneity rather than uniform stiffening. This heterogeneity can be rationalized by spatially non-uniform oxidation, moisture ingress, and local differences in stabilizer or surfactant distribution. Humidity-induced phase transitions of surfactants embedded in latex coatings have been shown to drastically alter mechanical properties and water barrier behavior, creating mechanically distinct nanoscale domains [51]. Such local compositional rearrangements may amplify stiffness gradients under weathering.

Hence, the weathered coating evolves from an initially homogeneous Young's modulus distribution toward a mechanically heterogeneous nanostructure characterized by stiff oxidized regions interspersed with comparatively compliant domains. Similar weathering-induced development of locally stiff regions has been reported in [14], who attributed the increase in local rigidity to the formation of polar oxidation products that promote stronger intermolecular interactions within the polymer network, and by [52], where thermal oxidation of a multiphase polymer similarly results in both a global increase in stiffness and a pronounced development of mechanical heterogeneity. Specifically, cross-linking in the rubbery phase leads to local stiffening, while concurrent chain scission in the glassy phase reduces molecular weight and promotes embrittlement. The coexistence of these competing mechanisms produces spatially distinct mechanical domains, reinforcing that the broadening of modulus distributions reflects heterogeneous degradation rather than uniform material evolution [52]. In the case of the present study, the connections between the former acrylate particles become weaker with increasing weathering time. On the other side, the highly entangled areas oxidize and become even stiffer, leading to an overall increase in Young's modulus.

In addition to ImAFM, bulk and nanoscale DMA have been performed to compare the storage modulus for bulk and surface properties. Fig. 6(b) depicts the resulting evolution of the storage modulus over accelerated weathering time. At first, the bulk and nanoscale DMA measurements coincide well. After two weeks of accelerated weathering time however, it is noticeable that the bulk storage modulus remains approximately constant but showing a higher spread within the measurement points compared to earlier degradation steps. The

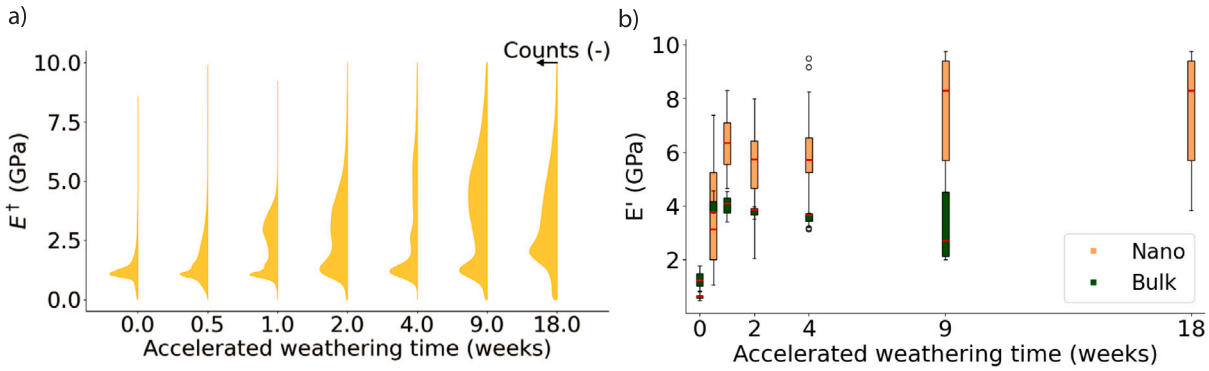


Fig. 6. (a) Effective young's modulus histogram evolution over accelerated weathering duration measured with ImAFM. For ImAFM every measured pixel corresponds to a calculated effective Young's-modulus. The number of counts (pixels) per effective Young's modulus are normalized for each sample and presented in the violin plot for each time point. With increasing weathering time the Young's modulus not only increases but also is spread more widely. (b) Storage modulus evolution over accelerated weathering time at 20 °C and approx. 150 Hz. Two different measurement methods are presented: Bulk DMA measurements as described in Section 2.4 and VEA as described in Section 2.3. With increasing accelerated weathering time the storage modulus increases.

nanoscale VEA measurements still show an increasing storage modulus. The formation of an oxidized "skin" layer could result in a pronounced gradient in chemical composition and mechanical properties across the film thickness, with a stiffened oxidized surface (see also Fig. 7) and a comparatively less degraded, more compliant subsurface [2]. This depth-dependent evolution is consistent with spectroscopic observations linking oxidation product formation to the progressive loss of reactive groups in the near-surface region under UV exposure [53]. Although the oxidation is a surface driven process, the whole coating became more brittle with accelerated weathering time as shown in the bulk DMA measurements, see the SI [17] Figure S3 (increasing T_g), and the increased standard deviation after nine weeks of accelerated weathering, cf. Section 2.3(b). Further, it was also noticeable for the sample handling. Following a period of nine weeks of accelerated weathering, the samples exhibited a marked increase in brittleness, making it challenging to detach them from their polypropylene substrates. The samples, which had undergone accelerated weathering for a period of 18 weeks, could not be detached due to their excessive fragility, hence, no bulk DMA measurements at 18 weeks were carried out. This finding aligns with the documented phenomenon of progressive embrittlement in free-standing films, as also reported in literature [54]. This increased brittleness suggests the presence of possible micro-cracks in the DMA samples, which may have contributed to premature failure and reduced stiffness. In this context, it has also been reported that conventional DMA measurements can have limited sensitivity in distinguishing different degradation states, particularly when mechanical damage influences the response [7]. This problem did not emerge in the nanoscale VEA measurements because the coating did not require detachment from the substrate, and no micro-cracks were observed during testing. This underscores the efficacy of implementing DMA at the nanoscale level, as it facilitates more efficient and dependable sample management. In summary it can be said that although the surface is mostly affected, the overall coating mechanical properties change with accelerated weathering time. Concurrently, the development of oxidized surface regions is associated with increased local rigidity, leading to a heterogeneous distribution of mechanical properties across the coating [53], which can also be observed in the present coatings. This behavior is further supported by Wärnheim et al. [14], who attributed weathering-induced increases in local stiffness to the formation of polar oxidation products, such as hydroxyl- and peracid-containing groups, which promote stronger intermolecular interactions through hydrogen bonding within the polymer network. Next to the increase in the OH/NH region and a decrease in the CH region, a broadening in the carbonyl band can be seen at the same time, characteristic of the disappearance of ester functionalities [55] and formation of

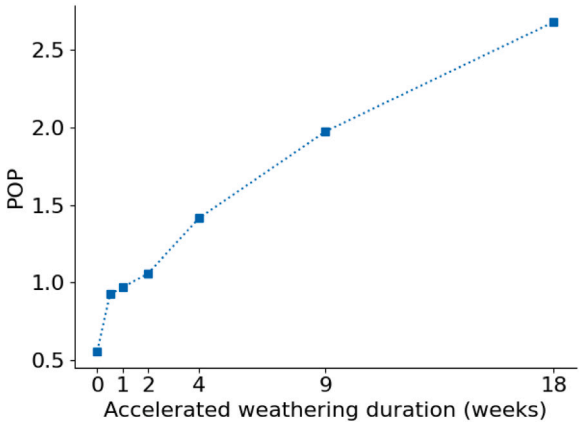


Fig. 7. FTIR measurements of the accelerated weather samples. With increasing weathering time the amount of photo-oxidation products (POP) increases which leads to more polar groups in the coating molecular structure. The inclusion of dashed lines in the diagrams is intended to facilitate the visual guidance of the reader's eye. For more details see Section 2.6.

new carbonyl compounds (ketones, carboxylic acids) [56,57], while the growth of a small band near 1781 cm^{-1} was also reported for weathered acrylic coatings as characteristic for cyclic lactones [58]. In the SI Figure S8 a close-up of the C=O region broadening induced by accelerated weathering can be found.

A comparison of the storage modulus increase due to only thermal aging with accelerated weathering is shown in the SI in Figure S9. It shows that already a significant stiffening of the samples is caused by thermal aging and hence, physical aging. It further reveals that the stiffness increase for accelerated weathering is more pronounced, indicating that the storage modulus increase caused by accelerated weathering is not only due to physical aging but also due to chemical changes, see Figure S9 in the SI. This is also supported by Fig. 7 which shows a quantifiable increase in surface oxidation products (as measured by FTIR-ATR) already after 0.5 weeks of exposure.

A summary of the proposed nanoscale degradation mechanism is sketched in Fig. 8. The first step shows the initial state of the cured coating. Due to the weathering cycle, the sample stiffens (step 2), which is attributed to the combined effects of physical aging and photo-oxidation. The presence of oxygen, water, and photo-degradation further induces degradation processes (step 3), which may contribute to the development of heterogeneous nanoscale mechanical domains

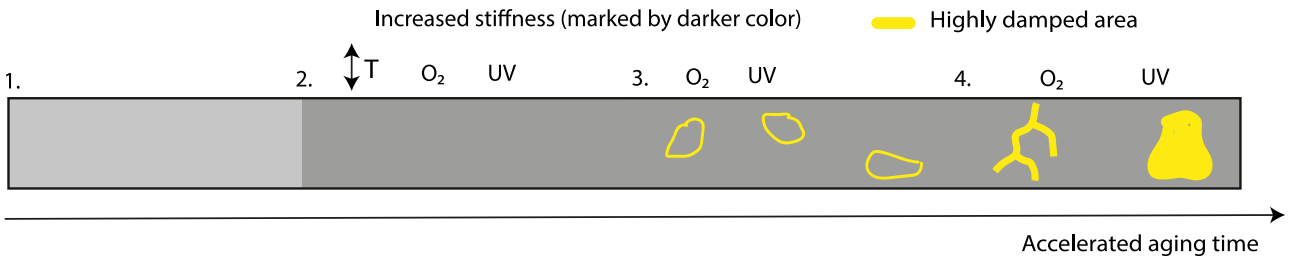


Fig. 8. Schematic representation of the proposed degradation evolution during accelerated weathering of a waterborne acrylate latex coating (top view; not to scale). The first step represents the initially homogeneous state after the curing process described in Fig. 1. During the accelerated weathering cycle, heating (step 2) induces physical aging and a corresponding increase in stiffness, which is overlapped by humidity-, UV-, and oxygen-induced degradation processes. Continued exposure to humidity, oxygen, and UV radiation promotes further degradation (step 3), resulting in the development of heterogeneous mechanical properties within the coating. The formation of mechanically distinct regions is schematically illustrated based on the observed increase in modulus heterogeneity and highly damped areas. These regions may be associated with degradation processes occurring preferentially in areas related to the former acrylate particle morphology, where reduced cohesion compared with the interior of the original particles may contribute to their formation. With increasing weathering time, the fraction and spatial distribution of these mechanically distinct regions increase (step 4), resulting in increasingly heterogeneous degradation. The localized highly damped regions may represent preferential pathways for failure initiation, contributing to the increasing brittleness observed with prolonged degradation. The schematic does not represent directly observed molecular structures or degradation domains, but illustrates a proposed interpretation of the experimentally observed chemical, topographical, and nanomechanical changes. In this schematic, UV exposure is oriented perpendicular to the coating surface. The viewer observes the coating surface, while the coating extends further into the paper direction.

and the appearance of features associated with the former acrylate particle morphology. The entanglement of polymer chains at the interface between particles is expected to be weaker than inside the original particles, and degradation in these regions may therefore result in reduced cohesion between former acrylate particles. This process may contribute to the formation of highly damped areas (illustrated in yellow). With increasing accelerated weathering time, a larger fraction of the coating is affected, and these mechanically distinct regions become more pronounced and spatially distributed across the former acrylate particle structure (step 4). Therefore, the degradation is heterogeneous, and the presence of highly damped areas may facilitate failure initiation. This phenomenon contributes to an increasing degree of brittleness as degradation time progresses.

4. Conclusion

In this study, we performed a comprehensive analysis of degradation in a waterborne acrylate coating by combining nanoscale measurement techniques (ImAFM and VEA) with commonly used characterization methods for assessing coating degradation. By correlating chemical, topographical, and nanomechanical information, a multi-stage degradation scenario is proposed:

1. **Stage 1 (0.5–4 weeks of accelerated weathering):** An overall increase in stiffness is observed, which is attributed to the combined effects of photo-oxidation and physical aging. The formation of oxidation products and the development of nanoscale mechanical heterogeneity indicate the onset of localized degradation processes. After approximately four weeks, gloss loss becomes macroscopically visible.
2. **Stage 2 (4–9 weeks of accelerated weathering):** Increasing mechanical heterogeneity is observed, characterized by the emergence of highly damped nanoscale regions and increasing contrast between stiff and compliant domains. For emulsion-based coatings, this behavior may be associated with degradation of interparticle bridge regions and reduced cohesion between previously coalesced particles. However, the present measurements do not directly resolve molecular disentanglement or interparticle bridge cleavage, and this interpretation should therefore be considered a proposed mechanism consistent with the observed mechanical evolution.
3. **Stage 3 (long-term, 18 weeks of accelerated weathering):** The continued evolution of mechanically heterogeneous regions is consistent with localized embrittlement and the development of preferential pathways for crack initiation and propagation [8], as described for weathered polymer coatings [2]. In the present study, regions associated with former acrylate particle boundaries may represent mechanically weakened pathways where degradation preferentially progresses.

These conclusions are based on measurements of the surface, where degradation starts. Further research on coatings cross-sections would have to confirm if the phenomena observed in the surface reflect what happens deeper inside the coating.

CRediT authorship contribution statement

L.V. Fricke: Writing – original draft, Visualization, Validation, Methodology, Investigation, Formal analysis, Data curation, Conceptualization. **N. Wansink:** Writing – review & editing, Validation, Software, Formal analysis. **M. Rosso:** Writing – original draft, Validation, Methodology, Investigation, Conceptualization. **G. van Ewijk:** Writing – review & editing, Validation. **M.P. Smak:** Data curation, Investigation. **P. Belardinelli:** Writing – review & editing, Software. **U. Staufer:** Writing – review & editing, Validation, Supervision, Funding acquisition. **F. Alijani:** Writing – review & editing, Validation, Supervision, Project administration, Funding acquisition, Conceptualization.

Declaration of competing interest

The authors declare the following financial interests/personal relationships which may be considered as potential competing interests: Farbod Alijani reports financial support was provided by Dutch Research Council. Michel Rosso reports a relationship with AkzoNobel that includes: employment. Gerard van Ewijk reports a relationship with AkzoNobel that includes: employment. If there are other authors, they declare that they have no known competing financial interests or personal relationships that could have appeared to influence the work reported in this paper.

Acknowledgments

This work was supported by the Netherlands Organization for Scientific Research (NWO) no. 19987. We thank Paul Markus for his continuous training in the use of the AFM.

Appendix A. Supplementary data

Supporting Information is available from the Elsevier Online Library or from the author [17].

Supplementary material related to this article can be found online at https://doi.org/10.1016/j.polymdegradstab.2026.112475.

Data availability

Data will be made available on request.

References

[1] K. Pieters, T.H. Mekonnen, Progress in waterborne polymer dispersions for coating applications: commercialized systems and new trends, RSC Sustain. 2 (2024) 3704–3729, http://dx.doi.org/10.1039/D4SU00267A.

[2] X.F. Yang, C. Vang, D.E. Tallman, B.G. P., S.G. Croll, S. Rohlik, Weathering degradation of a polyurethane coating, Polym. Degrad. Stab. 74 (2) (2001) 341–351, http://dx.doi.org/10.1016/S0141-3910(01)00166-5.

[3] X.F. Yang, D.E. Tallman, G.P. Bierwagen, S.G. Croll, S. Rohlik, Blistering and degradation of polyurethane coatings under different accelerated weathering tests, Polym. Degrad. Stab. 77 (1) (2002) 103–109, http://dx.doi.org/10.1016/S0141-3910(02)00085-X.

[4] D. Bergamasco, F. Bulian, A. Melchior, D. Menotti, P. Tirelli, M. Tolazzi, DMA analysis to predict the performance of waterborne coatings, J. Therm Anal. Calorim. 103 (2011) 65–68, http://dx.doi.org/10.1007/s10973-010-1160-7.

[5] T. Nguyen, X. Gu, M. Vanlandingham, E. Byrd, R. Ryntz, J.W. Martin, Degradation modes of crosslinked coatings exposed to photolytic enviroment, J. Coat. Technol. 10 (1) (2013) 1–14, http://dx.doi.org/10.1007/s11998-012-9455-1.

[6] M. Rosso, Outdoor durability of radiation-cured coatings – a review, Prog. Org. Coat. 210 (2026) 109642, http://dx.doi.org/10.1016/j.porgcoat.2025.109642.

[7] H.-C. Huang, D. Hunston, L. Sung, Exploration of dynamic mechanical analysis for studying degraded polymers: Dynamic mechanical changes after ultraviolet exposure, Polym. Degrad. Stab. 242 (2025) 111698, http://dx.doi.org/10.1016/j.polymdegradstab.2025.111698.

[8] S.G. Croll, Stress and embrittlement in organic coatings during general weathering exposure: A review, Prog. Org. Coat. 172 (2022) 107085, http://dx.doi.org/10.1016/j.porgcoat.2022.107085.

[9] B. Voogt, H.P. Huinink, S.J.F. Erich, J. Scheerder, P. Venema, J.L. Keddie, O.C.G. Adan, Film formation of high Tg latex using hydroplasticization: Explanations from NMR relaxometry, Langmuir 35 (38) (2019) 12418–12427, http://dx.doi.org/10.1021/acs.langmuir.9b01353.

[10] H. Abdeldaim, Effect of Particle Morphology on Film Cracking (Ph.D. thesis), Universidad del País Vasco, Donostia, Spain, 2023.

[11] A. Overbeek, Polymer heterogeneity in waterborne coatings, J. Coat. Technol. Res. 7 (2010) 1–21, http://dx.doi.org/10.1007/s11998-009-9201-5.

[12] A. Arjmandi, H. Bi, S.U. Nielsen, K. Dam-Johansen, From wet to protective: Film formation in waterborne coatings, ACS Appl. Mater. Interfaces 16 (43) (2024) 58006–58028, http://dx.doi.org/10.1021/acsami.4c09729.

[13] W. Schlesing, M. Buhk, M. Osterhold, Dynamic mechanical analysis in coatings industry, Prog. Org. Coat. 49 (3) (2004) 197–208, http://dx.doi.org/10.1016/j.porgcoat.2003.09.009.

[14] A. Wärnheim, N. Kotov, I. Dobryden, R. Telaretti Leggieri, C. Edvinsson, G. Heydari, P.-E. Sundell, T. Deltin, C.M. Johnson, D. Persson, P.M. Claesson, Nanomechanical and nano-FTIR analysis of polyester coil coatings before and after artificial weathering experiments, Prog. Org. Coat. 190 (2024) 108355, http://dx.doi.org/10.1016/j.porgcoat.2024.108355.

[15] B. Rajabifar, J.M. Jadhav, D. Kiracofe, G.F. Meyers, A. Raman, Dynamic AFM on viscoelastic polymer samples with surface forces, Macromolecules 51 (23) (2018) 9649–9661, http://dx.doi.org/10.1021/acs.macromol.8b01485.

[16] X. Zhang, S. Sun, N. Ning, S. Yan, X. Wu, Y. Lu, L. Zhang, Visualization and quantification of the microstructure evolution of isoprene rubber during uniaxial stretching using AFM nanomechanical mapping, Macromolecules 53 (8) (2020) 3082–3089, http://dx.doi.org/10.1021/acs.macromol.9b02656.

[17] Supporting Information, https://ars.els-cdn.com/content/image/1-s2.0-S0141391026005513-mmc1.pdf.

[18] H. Cao, R. Zhang, C.S. Sundar, J.-P. Yuan, Y. He, T.C. Sandreczki, Y.C. Jean, B. Nielsen, Degradation of polymer coating systems studied by positron annihilation spectroscopy. 1. UV irradiation effect, Macromolecules 31 (19) (1998) 6627–6635, http://dx.doi.org/10.1021/ma9802778.

[19] ISO, ISO 16474-2:2013 Paints and Varnishes — Methods of Exposure to Laboratory Light Sources, Standard, International Organization for Standardization, Geneva, CH, 2013.

[20] ISO, ISO 4892-2:2013 Plastics — Methods of Exposure to Laboratory Light Sources, Standard, International Organization for Standardization, Geneva, CH, 2013.

[21] Volkswagen, PV 3930 Non-Metallic Materials - Weathering in Moist, Hot Climate, Standard, Volkswagen AG, Wolfsburg, Germany, 2007.

[22] H.K. Nguyen, X. Liang, M. Ito, K. Nakajima, Direct mapping of nanoscale viscoelastic dynamics at nanofiller/polymer interfaces, Macromolecules 51 (15) (2018) 6085–6091, http://dx.doi.org/10.1021/acs.macromol.8b01185.

[23] S. Benaglia, C.A. Amo, R. Garcia, Fast, quantitative and high resolution mapping of viscoelastic properties with bimodal AFM, Nanoscale 11 (32) (2019) 15289–15297, http://dx.doi.org/10.1039/C9NR04396A.

[24] J.E. Sader, J.W.M. Chon, P. Mulvaney, Calibration of rectangular atomic force microscope cantilevers, Rev. Sci. Instrum. 70 (10) (1999) 3967–3969, http://dx.doi.org/10.1063/1.1150021.

[25] M.J. Higgins, R. Proksch, J.E. Sader, M. Polcik, S. Mc Endoo, J.P. Cleveland, S.P. Jarvis, Noninvasive determination of optical lever sensitivity in atomic force microscopy, Rev. Sci. Instrum. 77 (1) (2006) 013701, http://dx.doi.org/10.1063/1.2162455.

[26] D. Platz, E.A. Tholén, D. Pesen, D.B. Haviland, Intermodulation atomic force microscopy, Appl. Phys. Lett. 92 (15) (2008) 153106, http://dx.doi.org/10.1063/1.2909569.

[27] E.A. Tholén, D. Platz, D. Forchheimer, V. Schuler, M.O. Tholén, C. Hutter, D.B. Haviland, Note: The intermodulation lockin analyzer, Rev. Sci. Instrum. 82 (2) (2011) 026109, http://dx.doi.org/10.1063/1.3541791.

[28] D. Platz, D. Forchheimer, E.A. Tholén, D.B. Haviland, Interpreting motion and force for narrow-band intermodulation atomic force microscopy, Beilstein J. Nanotechnol. 4 (2013) 45–56, http://dx.doi.org/10.3762/bjnano.4.5.

[29] D. Silbernagl, A. Kömmling, M. Zaghdoudi, M. Ghasem Zadeh Khorasani, M. Jaunich, Data-driven nanomechanical study of filled fluoroelastomer aged in air and hydrogen atmosphere, Polym. Degrad. Stab. 242 (2025) 111715, http://dx.doi.org/10.1016/j.polymdegradstab.2025.111715.

[30] A. Chandrashekar, A. Givois, P. Belardinelli, C.L. Penning, A.M. Aragón, U. Staufer, F. Alijani, Sensitivity of viscoelastic characterization in multi-harmonic atomic force microscopy, Soft Matter 18 (2022) 8748–8755, http://dx.doi.org/10.1039/D2SM00482H.

[31] R. Garcia, C.J. Gómez, N.F. Martinez, S. Patil, C. Dietz, R. Magerle, Identification of nanoscale dissipation processes by dynamic atomic force microscopy, Phys. Rev. Lett. 97 (2006) 016103, http://dx.doi.org/10.1103/PhysRevLett.97.016103.

[32] A. Chandrashekar, P. Belardinelli, S. Lenci, U. Staufer, F. Alijani, Mode coupling in dynamic atomic force microscopy, Phys. Rev. Appl. 15 (2) (2021) 024013.

[33] R. García, R. Pérez, Dynamic atomic force microscopy methods, Surf. Sci. Rep. 47 (6) (2002) 197–301, http://dx.doi.org/10.1016/S0167-5729(02)00077-8.

[34] K. Menard, Dynamic Mechanical Analysis: A Practical Introduction, second ed., CRC Press, 2008, http://dx.doi.org/10.1201/9781420053135.

[35] R.M. Khan, M. Rejhon, Y. Li, N. Parashar, E. Riedo, R.R. Wixom, F.W. DelRio, R. Dingreville, Probing the mechanical properties of 2D materials via atomic-force-microscopy-based modulated nanoindentation, Small Methods 8 (3) (2024) 2301043, http://dx.doi.org/10.1002/smtd.202301043.

[36] R. Proksch, M. Kocun, D. Hurley, M. Viani, A. Labuda, W. Meinhold, J. Bemis, Practical loss tangent imaging with amplitude-modulated atomic force microscopy, J. Appl. Phys. 119 (13) (2016) 134901, http://dx.doi.org/10.1063/1.4944879.

[37] L.V. Fricke, N. Wansink, M. Rosso, U. Staufer, P. Belardinelli, F. Alijani, Probing viscoelasticity of polymeric coatings using nonlinear dynamic atomic force microscopy, Small Methods 10 (2) (2025) 2500723, http://dx.doi.org/10.1002/smtd.202500723.

[38] B. Pittenger, S. Osechinskiy, D. Yablon, T. Mueller, Nanoscale DMA with the atomic force microscope: A new method for measuring viscoelastic properties of nanostructured polymer materials, JOM 71 (10) (2019) 3390–3398, http://dx.doi.org/10.1007/s11837-019-03698-z.

[39] A.R. Piacenti, C. Adam, N. Hawkins, R. Wagner, J. Seifert, Y. Taniguchi, R. Proksch, S. Contera, Nanoscale rheology: Dynamic mechanical analysis over a broad and continuous frequency range using photothermal actuation atomic force microscopy, Macromolecules 57 (3) (2024) 1118–1127, http://dx.doi.org/10.1021/acs.macromol.3c02052.

[40] L.M. Rebêlo, J.S. de Sousa, J.M. Filho, J. Schäpe, H. Doschke, M. Radmacher, Microrheology of cells with magnetic force modulation atomic force microscopy, Soft Matter 10 (2014) 2141–2149, http://dx.doi.org/10.1039/C3SM52045E.

[41] ISO, ISO 2813:2014 Paints and Varnishes — Determination Of Gloss Value at 20°, 60° and 85°, Standard, International Organization for Standardization, Geneva, CH, 2014.

[42] ASTM, ASTM D523-14 Standard Test Method for Specular Gloss, Standard, ASTM International, West Conshohocken, USA, 2018.

[43] J.L. Keddie, A.F. Routh, Fundamentals of Latex Film Formation, in: Springer Laboratory, Springer Dordrecht, 2010, http://dx.doi.org/10.1007/978-90-481-2845-7.

[44] L.W. Hill, H.M. Korzeniowski, M. Ojunga-Andrew, R.C. Wilson, Accelerated clearcoat weathering studied by dynamic mechanical analysis, Prog. Org. Coat. 24 (1) (1994) 147–173, http://dx.doi.org/10.1016/0033-0655(94)85012-7.

[45] P. Vink, T.P.M. Koster, H.F.N. Fontijn, A. Mackor, UV stability of water-borne acrylic coatings, Polym. Degrad. Stab. 48 (1) (1995) 155–160, http://dx.doi.org/10.1016/0141-3910(95)00016-F.

[46] X. Gu, T. Nguyen, M. Oudina, et al., Microstructure and morphology of amine-cured epoxy coatings before and after outdoor exposures—An AFM study, J. Coat. Technol. Res. 2 (2005) 547–556, http://dx.doi.org/10.1007/s11998-005-0014-x.
[47] T.V. Nguyen, P. Nguyen Tri, T.D. Nguyen, R. El Aidani, V.T. Trinh, C. Decker, Accelerated degradation of water borne acrylic nanocomposites used in outdoor protective coatings, Polym. Degrad. Stab. 128 (2016) 65–76, http://dx.doi.org/10.1016/j.polymdegradstab.2016.03.002.
[48] M. Vlad-Cristea, B. Riedl, P. Blanchet, E. Jimenez-Pique, Nanocharacterization techniques for investigating the durability of wood coatings, Eur. Polym. J. 48 (3) (2012) 441–453, http://dx.doi.org/10.1016/j.eurpolymj.2011.12.002.
[49] E. Rull Trinidad, T.W. Gribnau, P. Belardinelli, U. Staufer, F. Alijani, Nonlinear dynamics for estimating the tip radius in atomic force microscopy, Appl. Phys. Lett. 111 (12) (2017) 123105, http://dx.doi.org/10.1063/1.4991471.
[50] S. Morsch, S. Lyon, S.D. Smith, S.R. Gibbon, Mapping water uptake in an epoxy-phenolic coating, Prog. Org. Coat. 86 (2015) 173–180, http://dx.doi.org/10.1016/j.porgcoat.2015.05.017.
[51] J.F. Gonzalez-Martinez, Y. Znamenskaya Falk, S. Bjorklund, S. Erkselius, N. Rehnberg, J. Sotres, Humidity-induced phase transitions of surfactants embedded in latex coatings can drastically alter their water barrier and mechanical properties, Polymers 10 (3) (2018) http://dx.doi.org/10.3390/polym10030284.
[52] C. Freymond, X. Mackré-Delannoy, A. Guinault, C. Charbuillet, B. Fayolle, Thermal oxidation of acrylonitrile-butadiene-styrene: Origin of the ductile/brittle transition, Polym. Degrad. Stab. 206 (2022) 110186, http://dx.doi.org/10.1016/j.polymdegradstab.2022.110186.
[53] L. Delarue, M.F. Pucci, L. Mercoiret, P. Ienny, P.-J. Liotier, A.-S. Caro-Bretelle, D. Perrin, Correlation between AFM characterizations and dynamic mechanical testing to assess the ductile-to-brittle transition during ABS photodegradation, Prog. Org. Coat. 220 (2024) 110945, http://dx.doi.org/10.1016/j.polymdegradstab.2024.110945.
[54] F. Steinberger, D. Hense, A. Rössler, O. Strube, Feasible estimation of weathering stability for free film acrylic coatings via dynamic mechanical analysis as the sole characterization method, J. Coat. Technol. Res. 22 (2) (2025) 839–848.
[55] V. Landry, P. Blanchet, Weathering resistance of opaque PVDF-acrylic coatings applied on wood substrates, Prog. Org. Coat. 75 (4) (2012) 494–501, http://dx.doi.org/10.1016/j.porgcoat.2012.06.004.
[56] C. Decker, K. Zahouily, Photodegradation and photooxidation of thermoset and UV-cured acrylate polymers, Polym. Degrad. Stab. 64 (2) (1999) 293–304, http://dx.doi.org/10.1016/S0141-3910(98)00205-5.
[57] C.-M. Popescu, B.C. Simionescu, Structural study of photodegraded acrylic-coated lime wood using Fourier transform infrared and two-dimensional infrared correlation spectroscopy, Appl. Spectrosc. 67 (6) (2013) 606–613, http://dx.doi.org/10.1366/12-06628.
[58] Y. Huang, Q. Feng, C. Ye, S.S. Nair, N. Yan, Incorporation of ligno-cellulose nanofibrils and bark extractives in water-based coatings for improved wood protection, Prog. Org. Coat. 138 (2020) 105210, http://dx.doi.org/10.1016/j.porgcoat.2019.105210.